International Journal of High Speed Electronics and Systems
Vol. 25, Nos. 3 & 4 (2016) 1640020 (9 pages)

DOI: 10.1142/S0129156416400206

Sub-Micron Gate Length Field Effect Transistors as Broad Band Detectors of Terahertz Radiation

J. A. Delgado Notario, E. Javadi*, J. Calvo-Gallego, E. Diez, J. E. Velázquez, and Y. M. Meziani[1]

NanoLab, Salamanca University, Pza. de la Merced, Edificio Trilingue, Salamanca, 37008, Spain
[1]meziani@usal.es

K. Fobelets

Department of Electrical and Electronic Engineering, Imperial College, London, Imperial College London, South Kensington Campus, London SW7 2AZ, UK

Received 12 November 2016
Accepted 28 November 2016

We report on room temperature non-resonant detection of terahertz radiation using strained Silicon MODFETs with nanoscale gate lengths. The devices were excited at room temperature by an electronic source at 150 and 300 GHz. A maximum intensity of the photoresponse signal was observed around the threshold voltage. Results from numerical simulations based on synopsis TCAD are in agreement with experimental ones. The NEP and Responsivity were calculated from the photoreponse signal obtained experimentally. Those values are competitive with the commercial ones. A maximum of photoresponse was obtained (for all devices) when the polarization of the incident terahertz radiations was in parallel with the fingers of the gate pads. For applications, the device has been used as a sensor within a terahertz imaging system and its ability for inspection of hidden objects was demonstrated.

Keywords: Si-MODFET; Terahertz detector; Plasma waves.

1. Introduction

The development of novel materials, concepts and device designs for terahertz radiation detection using semiconductors[1] has recently fueled the research of room temperature THz detectors. In early 90's, Dyakonov *et al.*[2,3] theoretically demonstrated the possibility of using sub-micron field effect transistors as detectors of terahertz radiation by means of the oscillations of plasma waves in their channel. Those devices present many advantages: low cost, small size, room temperature operation, and high speed response that make them highly competitive with other technologies. Room temperature detection of sub-terahertz radiation has been demonstrated by using different types of transistors such as commercial GaAs FETs[4] and Si-MOSFET.[5] An array of Si-MOSFETs was

*Also with: School of ECE, College of Engineering, University of Tehran, Tehran, Iran.

reported[6] with responsivity ~70 kV/W and NEP (Noise Equivalent Power) ~300 pW/Hz$^{1/2}$. Recently, asymmetric double grating gates devices based on GaInAS/InP HEMTs have shown a record of responsivity and NEP of around 20 kV/W and 0.48 pW/Hz$^{1/2}$, respectively.[7] Inspection feature of terahertz imaging has been demonstrated using those detectors.[5-8] New devices based on topological insulators[9] or graphene[10-11] are also investigated toward higher performance in terms of responsivity and NEP.

In the present work, we investigated room temperature terahertz detection using Strained Silicon Modulation field effect transistor (MODFET) with different gate lengths. Those devices are compatible with the main stream CMOS technology and do show higher mobility in comparison with CMOS ones. Experimental results show a good level of response to terahertz radiation at 150/300 GHz. Simulation results, based on 2D numerical studies using Synopsys TCAD,[12] show a non-resonant response in agreement with measurements. Very competitive values of parameters performance (NEP and responsivity) were obtained. Our device was used as a sensor within a THz imaging system and inspection of hidden objects was demonstrated.

2. Strained Silicon MODFET and TCAD Modeling

The material system Si/SiGe allows the creation of a thin layer of strained silicon under tetragonal (biaxial tensile) strain. This strain has significant implications for the band structure of the semiconductor.

Tetragonal strain has the effect of lifting the six-fold degeneracy of the conduction band in silicon into a two-fold and four-fold degenerate set. The deformation potential of the strain lowers the energy of the two valleys with their long axis perpendicular to the Si/SiGe interface. The amount of energy lowering is dependent on the degree of strain. It has been theoretically predicted[13] that approximately 0.8 % strain, resulting from a $Si_{0.8}Ge_{0.2}$ alloy, provides sufficient lowering that only the two-fold degenerate valleys are occupied at room temperature for low values of the electric field. Since intervalley carrier scattering may only occur between degenerate minima, electrons in a layer of (tensile) strained silicon would undergo a lower number of intervalley scattering events per unit time – a coniderable part of the intervalley scatterings that take place in a bulk material will vanish in strained Si as there are fewer possible final states for a carrier to scatter into – than in a similar layer of bulk silicon. The combination of lower scattering rates (higher values of the momentum relaxation time) and a lower value of the electron conductivity mass as compared to bulk Si makes tensile strained silicon layers excellent candidates to be used in high-mobility FET channels as the transport in those structures is parallel to the Si/SiGe interface.

The epistructure of the MODFETs used in this work was grown by molecular beam epitaxy (MBE) on a thick relaxed SiGe virtual substrate grown by low-energy plasma-enhanced chemical vapor deposition (LEPECVD) over a p-doped conventional Si wafer [Fig. 1(a)]. The final Ge molar concentration in the virtual substrate was $x_{Ge} = 0.45$. The device had a 12 nm tensile strained Si channel, sandwiched between two heavily doped SiGe electron supply layers to generate a high carrier density in the Strained-Si quantum

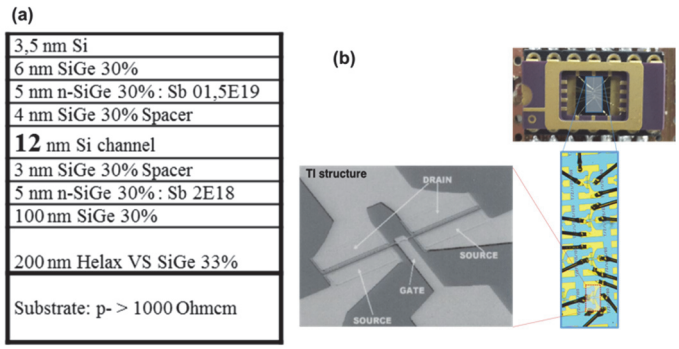

Fig. 1. (a) Epi-structure of devices (b) Ti-shape design and devices on DIL14 with a microscope image of the devices.

well;[12] to ensure high channel mobility spacers were used to reduce remote impurity scattering by dopants in the supply layers. The ohmic contacts were not self-aligned, the gate electrode was not symmetrically placed between source and drain. All devices had a Ti shape design [Fig. 1(b)] and were mounted on the same dual inline package (DIL14). Table 1 shows the geometrical parameters of tree transistors; typical transfer characteristics are presented in the inset of Figs. 3 and 4.

Owing to the nature of the carrier transport in submicron length gate devices, we used a hydrodynamic (2DHD) model for the majority carriers (electrons) self-consistently coupled to a two-dimensional solution of the Poisson equation.[14] Transport parameters for both holes and electrons were obtained by fitting uniform-field Monte Carlo results obtained for unstrained SiGe and for Si under tensile strain. In the 2DHD simulations impurity de-ionization, Fermi-Dirac statistics and mobility degradation due to both longitudinal and transverse electric field were taken into account. The source and drain regions were simulated as non-self-aligned implanted contacts.

Table 1. Geometrical parameters of the SiMODFETs.

	L_{SD} (μm)	L_g (nm)	W_{SD} (μm)
Device 1	2	100	80
Device 2	2	150	80
Device 3	2	500	80

The study of the THz photovoltaic response of the transistor is implemented by biasing source and gate and floating the drain contact while, as in measurements, a sub-THz sinusoidal signal was superimposed to the gate voltage as described in Refs. 2 and 3. The amplitude of the gate signal was fixed to 5 mV; the induced drain voltage exhibit both the same shape (sinusoidal) and frequency of the gate AC voltage ensuring that no frequency conversion takes place but its amplitude is considerably smaller than the one of the gate's signal as in the sub-THz range the device is unable to amplify signals, additionally the mean value of the induced drain voltage were negative in good agreement with theoretical models.[2,3]

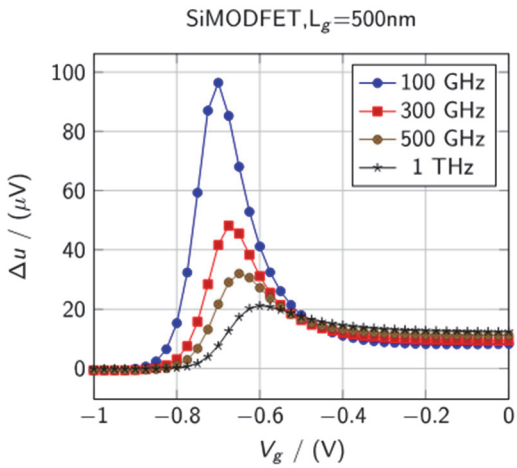

Fig. 2. Simulated photoresponse signal as a function of gate voltage for a device with L_g = 500 nm and under different frequency excitation (100, 300, 500 GHz, and 1 THz).

The charge boundary condition for the floating electrode was specified as:

$$\oint \vec{D}\vec{dS} = Q, \tag{1}$$

where $\vec{D}$ is the displacement vector, Q is the total charge and the integral is evaluated over the drain contact surface. A time-domain simulation was subsequently carried out to obtain the photovoltaic response (Fig. 2).

3. Results and Discussions

The devices were excited at room temperature by a dual-frequency electronic source based on frequency multipliers. The emission frequencies are 150 and 300 GHz with output power levels of 4 mW and 6 mW, respectively. The incoming radiation intensity was modulated by a mechanical chopper between 0.233 to 1.29 kHz and coupled to the device via the metallization pads and bounding wires. The induced photoresponse (Δu) signal was measured by using a lock-in technique. Typical obtained photoresponse signals vs. gate voltage are shown in Fig. 3 for device 1 with L_g = 100 nm under excitation of 150 (blue square symbol) and 300 GHz (blue dotted symbol). Figure 4 shows the case of device 3 with L_g = 500 nm under excitation of 150 GHz (blue square symbol) and 300 GHz (blue dotted symbol). For both cases, it's clearly seen the high value of the signal to noise ratio and a maximum intensity was observed around the threshold voltage. This behavior has been reported earlier and explained as non-resonant (broadband) detection due to low quality factor ($Q = \omega\tau < 1$)[15] i.e. low mobility in the device's channel. In the present case, the device shows higher channel mobility (~1300 cm^2/V·s) as compared to the conventional Si-MOSFET (~200 cm^2/V·s) the quality factor was estimated around 0.13 at f = 150 GHz and ~0.27 at f = 300 GHz and do not reach the resonance condition.

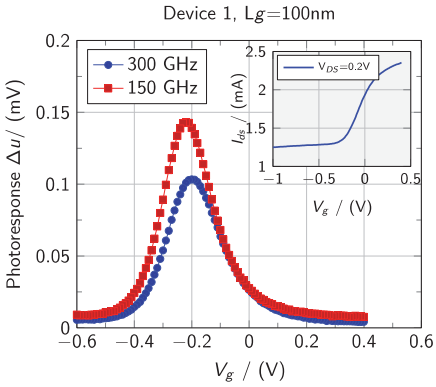

Fig. 3. Photoresponse vs. gate voltage under excitation of 150 GHz (red square) and 300 GHz (blue dotted) for Device 1 with L_g = 100 nm. Inset shows the corresponding transfer characteristics.

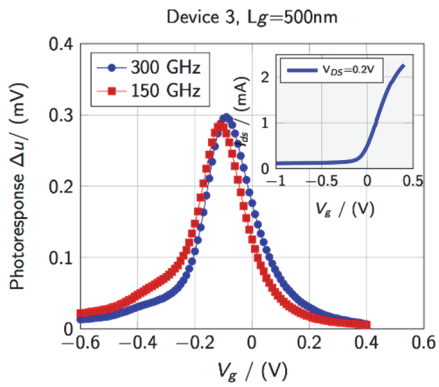

Fig. 4. Photoresponse vs. gate voltage under of 150 GHz (red square) and 300 GHz (blue dotted) for Device 4 with L_g = 500 nm. Inset shows the corresponding transfer characteristics.

Responsivity as well as the Noise Equivalent Power (NEP) are the key parameters to determine the performance of this detectors. The NEP is given by: N_{th}/R_V, where N_{th} is the thermal noise of the transistor in V/Hz$^{0.5}$ and R_V is the responsivity in V/W. Since detection was studied at zero drain bias the thermal noise $N_{th} = (4kTR_{ds})^{0.5}$ was the only source of noise of the transistor. Here R_{ds} is the drain-to-source resistance, which was extracted from the transfer characteristics measured at low drain bias corresponding to the linear regime (inset of Figs. 3 and 4). The responsivity is given as: $R_v = \Delta u \cdot S_t /(P_t \cdot S_a)$, where Δu is the measured photoresponse, S_t is the radiation beam spot area, S_a the active area, and P_t the total incident power surrounding the detector. The radiation beam power at the detector position was estimated to be around 0.5/1 mW at 150/300 GHz, respectively. The spot area S_t is given by πr^2 where r is the radius of the beam spot (≈ 1.5 mm @ 300 GHz and 3.3 mm @ 150 GHz). Since the area of both transistors with contact pads [Fig. 1(b)] was much smaller than the diffraction limit area $S_\lambda = \lambda^2/4$, the active area was taken equal to S_λ. Figure 4 shows the NEP = N_{th}/R_V for device 1 under excitation of 150 (blue dotted) and 300 GHz (red square). As seen, the device shows a minimum NEP around the threshold voltage. Therefore, the NEP_{min} and maximum responsivity ($R_{v\text{-max}}$) for this device are: at 150 GHz, NEP_{min} ~ 150 pW/Hz$^{0.5}$, $R_{v\text{-max}}$ ~ 10 V/W and at 300 GHz, NEP ~ 500 pW/Hz$^{0.5}$, R_v ~ 3 V/W.

Table 2 summarizes the obtained NEP and R_v for the remaining studied devices at 150 and 300 GHz. Device 2 with L_g = 150 nm shows the best performance at 150 GHz where: $R_{v\text{-max}}$ ~ 15V/W @ 150 GHz and NEP_{min} ~ 150 pW/Hz$^{0.5}$. This must be attributed to the large photoresponse signal exhibited by this device and to a better coupling with the incoming terahertz radiation. Those obtained values of NEP and responsivity are comparable to the commercial room temperature terahertz detectors like golay cell, pyroelectric detector, and Schottky diode. However, the Si-MODFET presents the advantage of working at higher modulation frequency.

Table 2. Calculated NEPs and R_v for different devices.

	150 GHz		300 GHz	
	NEP (pW/Hz$^{0.5}$)	R_v (V/W)	NEP (pW/Hz$^{0.5}$)	R_v (V/W)
Device 1	158	9.8	520	3
Device 2	125	15	546	3.6
Device 4	400	9.8	430	8.5

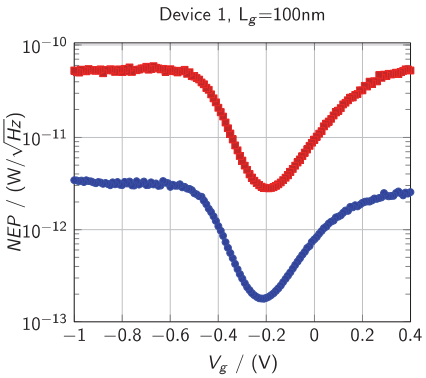

Fig. 5. Noise equivalent power as a function of the gate voltage of Device 1 under different THz excitations: 150 GHz (blue dotted), 300 GHz (red square), $T = 300$ K.

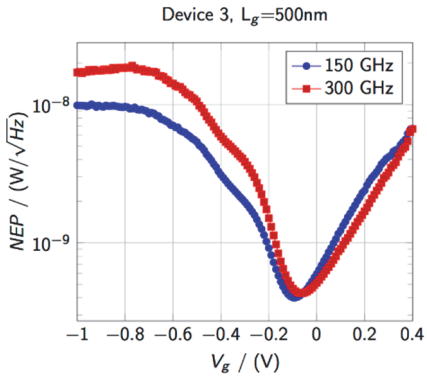

Fig. 6. Noise equivalent power as a function of the gate voltage of Device 4 under different THz excitations: 150 GHz (blue dotted), 300 GHz (red square), $T = 300$ K.

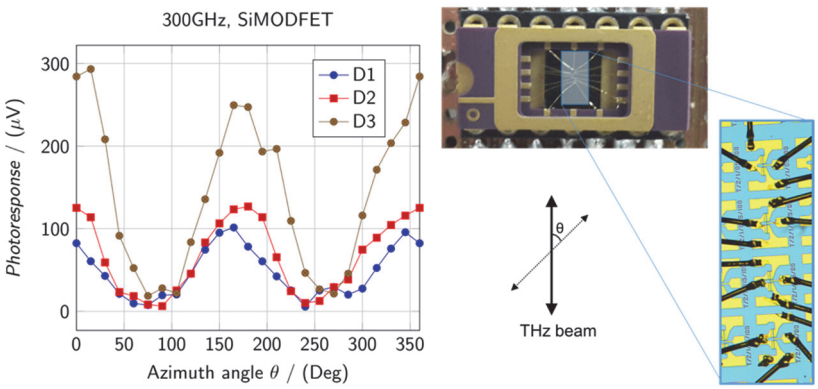

Fig. 7. Photoresponse vs. rotation angle for all devices under excitation of 300 GHz. Inset shows the devices mounted on dual in line package and at 0º where polarisation of THz beam is parallel to the gates pads.

The bonding wires and the metallic pads could play an antenna role to couple the incoming terahertz radiation to the 2D electron channel.[16-18] Sakowicz *et al.*[17] have shown that at low frequencies the radiation is coupled to the transistor mainly by bonding wires, whereas at higher frequencies (> 100 GHz) the metallization of the contact pads plays the role of efficient antennas. Figure 7 shows the photoresponse signal as a function of the polarization of the incoming THz radiation (linearly polarized). In measurements, the

device was rotated in the plane perpendicular to the terahertz beam and the photoresponse signal was measured for each angular position of the device. All devices were mounted on the same dual in line package (Fig. 7) and under excitation of 300 GHz. A maximum intensity signal was obtained around the threshold bias for each angle. It is clearly seen for all the devices, that a maximum of the signal results when the incoming radiation is parallel to the gate fingers pads. We can conclude that to maximize the detection of THz signals these must be polarized in a direction parallel to the gate pads.

4. Terahertz Imaging

To demonstrate their use for practical applications, the detector was used as a sensor within a terahertz imaging system. The emitted radiation from the source at 150 and 300 GHz was collimated and focused through different off-axis parabolic mirrors. The image was collected in transmission mode. A visible red LED in combination with an indium tin oxide (ITO) mirror are used for the alignment of the terahertz beam. More information about the terahertz imaging system setup can be found in Ref. 8. The radiation passes through the hidden object and the intensity measured by the device biased around the threshold voltage for maximum intensity of the signal. Figure 8 shows the terahertz images obtained at 150 and 300 GHz as well as the visible one. Better resolution was obtained at 300 GHz which is related to lower wavelength (λ = 1 mm). A clear terahertz image of the inspected object was observed.

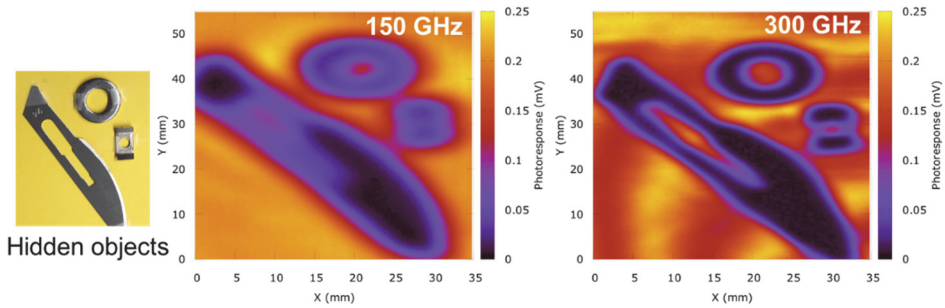

Fig. 8. Visible image (left) and terahertz ones (right) at 150/300 GHz obtained at room temperature with Device 4 with L_g = 500 nm.

5. Conclusion

We report on non-resonant detection of terahertz radiation at 150 and 300 GHz at room temperature by using strained-Si MODFETs with different gate lengths. Simulation results, based on 2D numerical studies with Synopsys TCAD, show a non-resonant response in agreement with measurements. Competitive values of the performance parameters (NEP and responsivity) were obtained. We have shown that in this case the gate pads are playing the role of antennae to couple the THz radiation to the 2D electron channel. For practical use of those detectors, a terahertz imaging for inspection of hidden objects was demonstrated.

Acknowledgments

This work was financially supported by the MINECO/FEDER Research Grant #TEC2015-65477-R and FEDER/Junta de Castilla y León Research Grant #SA045U16. Authors thank Dr. W. Knap and D. But from Teralab at Montpellier 2 University for calibration of our detectors. Y. M. Meziani acknowledges the financial support from RIEC nation-wide Collaborative Research Project, Sendai Japan.

References

1. M. Tonouchi, "Cutting-edge terahertz technology", *Nat. Photon*. **1** (2007) 97–105.
2. M. Dyakonov and M. S. Shur, "Shallow water analogy for a ballistic field effect transistor: New mechanism of plasma wave generation by dc current", *Phys. Rev. Lett*. **71** (1993) 2465.
3. M. Dyakonov and M. S. Shur, "Mixing, and frequency multiplication of terahertz radiation by two dimensional electronic fluid", *IEEE Trans. Electron Dev.* **43** (1996) 380.
4. W. Knap, Y. Deng, S. Rumyantsev, J. Q. Lu, M. S. Shur, C. A Saylor, and L. C. Brunel, "Resonant detection of subterahertz radiation by plasma waves in a submicron field-effect transistor", *Appl. Phys. Lett.* **80** (2002) 3433.
5. R. Tauk, F. Teppe, S. Boubanga, D. Coquillat, W. Knap, Y. M. Meziani, C. Gallon, F. Boeuf, T. Skotnicki, C. Fenouillet-Beranger, D. K. Maude, S. Rumyantsev, and M. S. Shur, "Plasma wave detection of terahertz radiation by silicon field effects transistors: Responsivity and noise equivalent power", *Appl. Phys. Lett.* **89** (2006) 253511.
6. A. Lisauskas, U. Pfeiffer, E. Öjefors, P. H. Bolìvar, D. Glaab, and H. G. Roskos, "Rational design of high-responsivity detectors of terahertz radiation based on distributed self-mixing in silicon field-effect transistors", *J. Appl. Phys.* **105** (2009) 114511.
7. T. Otsuji, "Trends in the research of modern terahertz detectors: plasmon detectors", *IEEE Trans. Terahertz Sci. Technol.* **5(6)** (2015) 1110–1120.
8. Y. M. Meziani, E. García-García, J. E. Velázquez-Pérez, D. Coquillat, N. Dyakonova, W. Knap, I. Grigelionis, and K. Fobelets, "Terahertz imaging using strained-Si MODFETs as sensors", *Solid-State Electron.* **83** (2013) 113–117.
9. L. Viti, D. Coquillat, A. Politano, K. A. Kokh, Z. S. Aliev, M. B. Babanly, O. E. Tereshchenko, W. Knap, E. V. Chulkov, and M. S. Vitiello, "Plasma-wave terahertz detection mediated by topological insulators surface states", *Nano Lett.*, **16** (2016) 80–87.
10. A. Zak, M. A. Andersson, M. Bauer, J. Matukas, A. Lisauskas, H. G. Roskos, and J. Stake, "Antenna-integrated 0.6 THz FET direct detectors based on CVD graphene", *Nano Lett.* **14(10)** (2014) 5834–5838.
11. L. Vicarelli, M. S. Vitiello, D. Coquillat, A. Lombardo, A. C. Ferrari, W. Knap, M. Polini, V. Pellegrini, and A. Tredicucci, "Graphene field-effect transistors as room-temperature terahertz detectors", *Nat. Mater.* **11(10)** (2012) 865–871.
12. Synopsys, Taurus User Guide, Version Z-2007.3 Synopsys Inc., Mountain View, CA (2007).
13. S. Takagi, J. L. Hoyt, J. J. Welser, and J. F. Gibbons, "Comparative study of phononlimited mobility of two dimensional electrons in strained and unstrained Si metal–oxide–semiconductor field effect transistors", *J. Appl. Phys.* **80** (1996) 1567-1577.
14. J. E. Velazquez, K. Fobelets, and V. Gaspari, "Study of current fluctuations in deep-submicron Si/SiGe n-channel MOSFET: impact of relevant technological parameters on the thermal noise performance", *Semicond. Sci. Technol*. **19** (2004) S191–S194.
15. W. Knap, F. Teppe, Y. Meziani, N. Dyakonova, J. Lusakowski, F. Boeuf, T. Skotnicki, D. Maude, S. Rumyantsev, and M. S. Shur, "Plasma wave detection of sub-terahertz and terahertz radiation by silicon field-effect transistors", *Appl. Phys. Lett.* **85** (2004) 675–677.

16. C. Drexler, N. Dyakonova, P. Olbrich, J. Karch, M. Schafberger, K. Karpierz, Y. Mityagin, M. B. Lifshits, F. Teppe, O. Klimenko, Y. M. Meziani, W. Knap, and S. D. Ganichev, "Helicity sensitive terahertz radiation detection by field effect transistors", *J. Appl. Phys.* **111** (2012) 124504.
17. M. Sakowicz, J. Lusakowski, K. Karpierz, M. Grynberg, W. Gwarek, S. Boubanga, D. Coquillat, W. Knap, A. Shchepetov, and S. Bollaert**,** "A high mobility field-effect transistor as an antenna for sub-THz radiation", *AIP Conf. Proc*. **1199** (2010) 503–504.
18. D. B. Veksler, A. V. Muravjov, V. Yu. Kachorovskii, T. A. Elkhatib, K. N. Salama, X. -C. Zhang, and M. S. Shur, "Imaging of field-effect transistors by focused terahertz radiation", Solid-State Electron. **53(6)** (2009) 571–573.